X-ray spectroscopic studies of the electronic density and temperature profiles in the transport region of 0.53- and 0.26-μm laser plasmas

P. Alaterre and C. Chenais-Popovics
Groupement de Recherches Coordonnées Interaction Laser Matière and Laboratoire de Physique des Milieux Ionisés, Ecole Polytechnique, 91128 Palaiseau Cédex, France

P. Audebert, J. P. Geindre, and J. C. Gauthier
Groupement de Recherches Coordonnées Interaction Laser Matière and Institut d'Electronique Fondamentale Bât. 220, Université Paris-XI, 91405 Orsay Cédex, France
(Received 12 September 1984; revised manuscript received 2 January 1985)

We present the first space-resolved experimental determination of electronic density and temperature profiles in the transport region for plane target irradiation with 400—600-ps pulses at 0.53- and 0.26-μm wavelengths, and $(1-3)\times10^{14}$-W/cm^2 laser intensity. The experimental technique is x-ray spot spectroscopy on thin Al microdots deposited on a carbon substrate. A knife-edge imaging technique ensures a spatial resolution of 3 μm along the laser axis. The electronic density and temperature are deduced from Stark broadening and intensity ratios of Al^{11+} and Al^{12+} $n=4$ resonance lines, respectively. The experimental profiles are well reproduced by one-dimensional spherical simulations including nonlocalized thermal flux inhibition or very low inhibition.

I. INTRODUCTION

X-ray spectroscopy of low-Z H-like and He-like ions has proved to be a powerful diagnostic method of the transport region in laser-produced plasmas.[1—4] Indeed, the emission of these ions is strongly peaked in the 0.6—1-keV electron temperature, high-density conduction region. The profiles and the intensity ratios of resonance lines and of dielectronic satellites are very sensitive to density and temperature variations. Due to steep gradients and fast expansion, spectral, spatial, and temporal resolution together with homogeneity of the plasma along the line of sight of the spectrograph are crucial problems for these diagnostics. In the present work we use spot spectroscopy[5] to ensure good spectral resolution and radial homogeneity of the emitting region, the targets being composed of embedded aluminum dots on a carbon substrate. 3-μm spatial resolution along the laser axis is obtained by inserting an imaging knife edge very close to the plasma.[6] In addition, the use of thin aluminum dots as targets shortens the duration of x-ray emission to control time integration effects.

In this paper we apply these techniques to measure the electron density and temperature profiles in the transport region of a plasma created by a 0.53- or 0.26-μm wavelength laser at intermediate intensities $[(1-3)\times10^{14}$ W/cm$^2]$ and compare them to one-dimensional (1D) hydrocode simulations. In Sec. II we describe the experimental conditions and the hydrocode parameters. Section III is devoted to a discussion of the validity conditions of the diagnostics, in particular time integration effects. In Sec. IV we show the experimental data and compare them to the simulations in Sec. V. Conclusions are found in Sec. VI.

II. PLASMA CONDITIONS AND COMPUTER MODELING

Experiments have been performed at the Groupement de Recherches Coordonnées Interaction Laser Matière (GRECO ILM) laser facility. We studied the interaction of a 400—600-ps pulse duration Nd:glass laser at 0.53- and 0.26-μm wavelengths with a plane carbon target embedded with 30—100-μm-diam aluminum dots. Rough time resolution was provided by the use of aluminum layers with a thickness close to the ablation depth. We chose 1.3- and 0.9-μm layers for 0.53- and 0.26-μm wavelength shots, respectively. Typical laser energies were 25 J at 0.53-μm and 10 J at 0.26-μm wavelength. Maximum laser intensities were 3×10^{14} and 1×10^{14} W/cm^2, respectively. Laser intensity was varied by defocusing the $f/3$ lens.

The centering of the tracer dots on the focal diameter was controlled by a pinhole camera. X-ray emission of Al^{11+} and Al^{12+} ions were recorded with a multiposition flat pentaerythritol (PET) crystal spectrograph covering a 3—8-Å range with 3—5-mÅ spectral resolution. The line of sight of the spectrograph made an angle of 7° with respect to the target surface in order to avoid x-ray-emission shielding by the edge of the target. An imaging knife edge was positioned between the plasma and the spectrograph slit at 0.5 or 1 mm from the laser axis providing an integrated image magnified 150 times. The parallelism of the knife edge with respect to the target surface was verified at each shot by superposing the spatial emissivity profiles of He-like lines and the underlying He-like continuum of H-like lines. Associated with computer deconvolution, this technique provides 3-μm spatial resolution along the laser axis. More details on the decon-

volution process can be found in Refs. 6 and 7.

Typical spectra showing the Al^{11+} Rydberg series and the $n=3$ resonance line of Al^{12+} are shown in Fig. 1. From the bottom to the top, the spectra are integrated from the target surface outwards to different positions along the laser axis (3, 6, 9, 12, and 15 μm). Spectra close to the target are emitted by the denser part of the plasma and exhibit typical Stark line broadening (Al^{11+} $n=4$ in particular). Away from the target, the electron density is decreasing and the lines get thinner. The figure shows also that H-like lines are emitted at larger distances from the target than He-like lines: At a distance of 3 μm from the target, the H-like line is negligible and the variation of the ratio of Al^{11+} $n=4$ to Al^{12+} $n=3$ lines is clearly seen. This is characteristic of the presence of an electron temperature gradient.

In the present study we have extensively used our 1D hydrodynamic code FILM to optimize the plasma conditions and to compare with the measured data. We used the version of the code which describes the ionic populations by a time-dependent collisional-radiative model including ladderlike ionization and recombination through excited states by a quasi-steady-state model.[8] The laser absorption process is inverse bremsstrahlung which is dominant for green and uv laser light. At 0.53-μm wavelength, we assumed that 30% of the energy reaching the critical density goes into 6-keV fast electrons.[9] For the uv case, we did not include fast electrons. Thermal conduction was described either by a delocalized theory[10] or by the usual flux-limited conductivity. In this case the heat flux is the quadratic mean value of the limited free streaming and the Spitzer-Härm values. We used either planar or spherical geometry. In this last case the target was a 150-μm-radius aluminum microsphere. The laser pulse duration has been fixed to 600 ps for 0.53-μm wavelength and 450 ps for uv light.

III. DETERMINATION OF THE ELECTRONIC DENSITY AND TEMPERATURE

A. Density

The electronic density is determined from the Stark broadening of $n=4$ lines of the Lyman series of Al^{11+} and Al^{12+}. These lines are well resolved from the recombination continuum and are less sensitive to reabsorption than the lines of lower quantum number. They will be respectively referred to as He_γ and H_γ hereafter. To obtain a whole density profile along the laser axis, several steps are necessary. First, we compare to a theoretical line profile[11] the data measured at the position along the laser axis where the maximum of emissivity is obtained. This theoretical profile includes a rough estimate of ion dynamics effects[12] and is convoluted with Doppler and instrumental profiles. For Al^{11+} lines, we use the Stark profiles calculated for magnesium H-like lines. The optical depth (i.e., the product of the absorption coefficient at line center by the photon path length) is considered as an adjustable parameter. The best fit of the experimental profile provides the electronic density and the optical depth. Figure 2 shows such an adjustment. The experimental data correspond to the He_γ line measured for a 0.53-μm wavelength, 3×10^{14}-W/cm^2 laser shot. They are compared with two theoretical profiles calculated for an optical depth $\tau=1.5$ and two electron densities $(2-3)\times10^{22}$ cm^{-3}. The figure shows that profile asymmetries add some uncertainty to the density determination. However, direct profile comparison gives a good estimate of the optical depth.

The whole electron density gradient is obtained by measuring the width of each line profile for several spatial

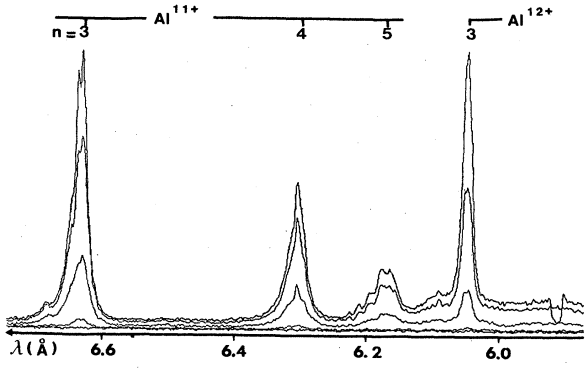

FIG. 1. Examples of He-like and H-like aluminum resonance line spectra obtained with the knife-edge technique (laser conditions: 0.53-μm wavelength; 3×10^{14}-W/cm^2 incident energy). n is the principal quantum number of the upper level. The different spectra are integrated from the target outwards to different positions along the laser axis (3, 6, 9, 12, and 15 μm from the bottom to the top).

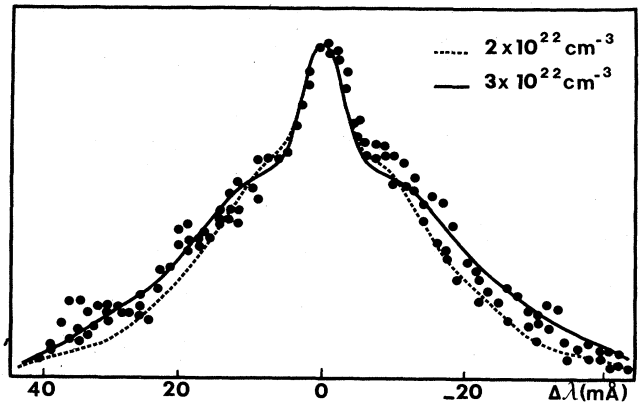

FIG. 2. Line profile of Al^{11+} $n=4$ line (He_γ). Circles: experimental profile measured in a 0.53-μm—3×10^{14}-W/cm^2 laser shot. Lines: theoretical profiles including Stark, Doppler, and instrumental broadening, opacity effects, and ion dynamics. This best fit is obtained with an optical depth at line center of 1.5.

positions along the laser axis. This is done through a numerical fit to a Gaussian or an asymmetric Lorentzian line shape. A preliminary calibration using the same kind of fit on the theoretical line profiles provides the correspondence between the full line width and the electron density. The optical depth of the line is included for this calibration. It is extrapolated from a few measurements done with direct comparison of experimental and theoretical profiles, as described in the preceding paragraph. This method gives the electronic density gradient shape with about 30% precision and 3-μm spatial resolution. More accurate density measurements can be obtained by a detailed analysis of several lines of a Rydberg series.[1,4,13] However, in our case where a large amount of data is to be treated, the present method was found more convenient and less computer time consuming.

B. Temperature

We deduce the electronic temperature from the intensity ratio of the $n=4$ lines of Al^{11+} and Al^{12+}. The validity of this classical method[14] is to be justified in the transient, out-of-equilibrium plasma under study. We have used the numerical simulations to test this validity and to evaluate the precision of the measurements. The line intensity ratio is proportional to the ratio of the populations of the bare and hydrogenic ions N_P and N_H:

$$I_{H_\gamma}/I_{He_\gamma}=(f_{H_\gamma}/f_{He_\gamma})(g_H^2/g_P g_{He}) \times(\lambda_{He_\gamma}/\lambda_{H_\gamma})^3(N_P/N_H)\,, \quad (1)$$

where f is the oscillator strength of a transition, g is the statistical weight of the fundamental level of the ion, and λ is the wavelength of the transition. He, H, and P refer, respectively, to heliumlike, hydrogenlike, and bare ions.

The temperature and density dependence of the N_P/N_H ratio are given by a collisional-radiative equilibrium (CRE) model. Figure 3 shows that N_P/N_H is only weakly dependent on electron density (we will neglect this dependence in the present study) but strongly temperature dependent in the 0.2—2-keV range.

In writing Eq. (1), we have assumed that the $n=4$ levels are in partial local thermodynamic equilibrium (partial LTE) with the upper ion stage. This is justified since, for the high-electron densities considered here, the collisional rates greatly exceed the radiative rates for transitions between high quantum number levels. We have also assumed that He_γ and H_γ lines have the same opacity. This is likely to be valid as we have measured low reabsorption on these lines. However, we have checked the corresponding maximum error on the temperature measurement. Detailed theoretical calculations are given in the Appendix. They show that reabsorption effects are negligible in the outer part of the plasma (at the H_γ maximum emission and outwards) and that the ratio $I_{H_\gamma}/I_{He_\gamma}$ is multiplied by no more than a factor of 2 in the He_γ emitting zone. As shown in Fig. 3, a factor of 2 in N_P/N_H corresponds to a maximum overestimate of 60 eV in the electron temperature of the He_γ emitting zone (around 500 eV), that is, about 12%. This error concerns mainly the part of the spatial profile close to the target. This will be included in the error bars.

The use of a steady-state model to link the ionic populations to the temperature can certainly be questioned. Taking into account a delay of the ionization would lead to a smaller N_P/N_H ratio for a given temperature. As our code includes the ionization dynamics of the ground levels, we used it to estimate the error made in deducing the electron temperature from the line intensity ratio with a CRE model. We computed at different times of the simulation (laser pulse maximum ± 100 ps) the ratio N_P/N_H as a function of electron temperature. Then, we used the CRE model depicted in Fig. 3 to deduce from this ratio a "diagnostic" temperature. Figure 4 shows the diagnostic temperature as a function of the electron tem-

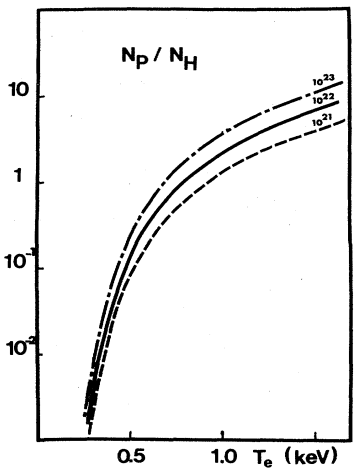

FIG. 3. Collisional radiative equilibrium of aluminum: ratio of the populations of the bare and hydrogenic ions as a function of electron temperature, calculated for three different electron densities, i.e., 10^{21}, 10^{22}, and 10^{23} cm^{-3}.

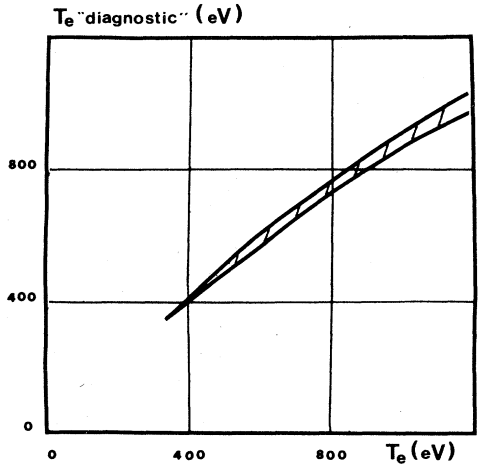

FIG. 4. Code simulation for 0.53-μm—3×10^{14}-W/cm^2 laser conditions. The "diagnostic" temperature calculated with a CRE model from the population ratio N_P/N_H is plotted vs the temperature around the laser pulse maximum. The dashed area represents the variations in a time interval of 200 ps centered on the laser pulse maximum.

perature calculated in the simulation. As expected with an ionization delay, the diagnostic temperature is lower than the simulation temperature. The difference is about 20% at high-temperature values, but a better agreement is found for the lower values. Taking into account the error due to reabsorption as mentioned above, we can expect the temperature measured from the line intensity ratio to be about 20% lower than the real temperature of the plasma.

C. Time integration effects

We adjust the thickness of the target to shorten the emission duration and to minimize the time integration of the emissivities. Figure 5 shows the time dependence of the He_γ and H_γ emissivities for two irradiation conditions: 1.3-μm- and 0.9-μm-thick aluminum layers irradiated, respectively, by a 0.53-μm-3×10^{14}-W/cm^2 and a 0.26-μm-1×10^{14}-W/cm^2 laser pulse. The emission duration is roughly the same as the laser pulse duration and emission occurs very close to the laser maximum. One can notice that the H-like emissivity is slightly delayed with respect to the He-like emissivity (less than 100 ps in all the calculated conditions).

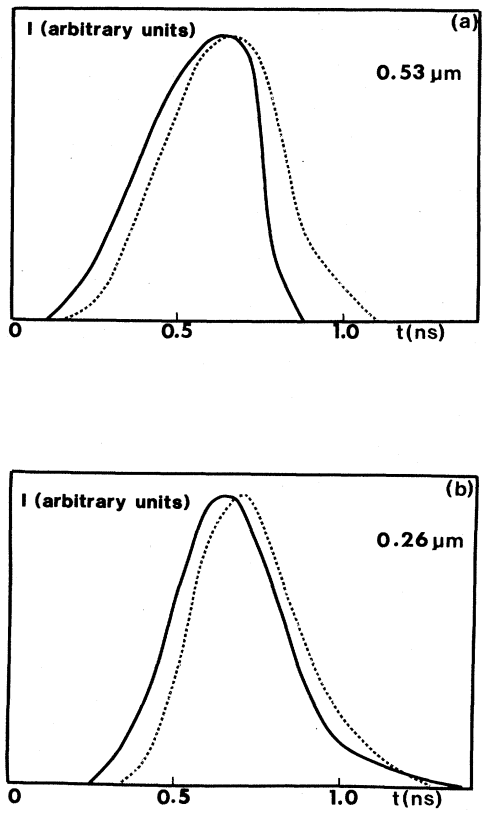

FIG. 5. Calculated time dependence of He_γ and H_γ emissivities. Solid line: He_γ emissivity. Short-dashed line: H_γ emissivity. (a) and (b) correspond to different simulation conditions: (a) 0.53-μm-3×10^{14}-W/cm^2 incident intensity, 1.3-μm Al thickness; (b) 0.26-μm-1×10^{14}-W/cm^2 incident intensity, 0.9-μm Al thickness.

We calculated the effect of this time duration and delay on the measured density and temperature. This is shown, respectively, in Figs. 6(a) and 6(b) for 0.53-μm-3×10^{14}-W/cm^2 laser irradiation. Figure 6(a) represents the density profiles around the laser pulse maximum ($\Delta t=-100$, 0, $+100$ ps) and the time integrated density weighted by the emissivities of He_γ and H_γ lines defined by

$$\langle n_e \rangle_{\mathrm{H,He}}(z)=\int n_e(t,z)I_{\mathrm{H,He}}(t,z)dt \Big/ \int I_{\mathrm{H,He}}(t,z)dt \ ,$$

where z is the coordinate along the laser axis.

This "weighted" density corresponds to what is actually measured by Stark broadening diagnostics. As can be seen in Fig. 6(a), it gives results very close to the real density gradient shape. As expected, the H_γ weighting gives a slightly lower density value due to the delay of the H_γ emissivity.

Figure 6(b) shows the "diagnostic temperature" gradient, deduced from the ratio of the time integrated line

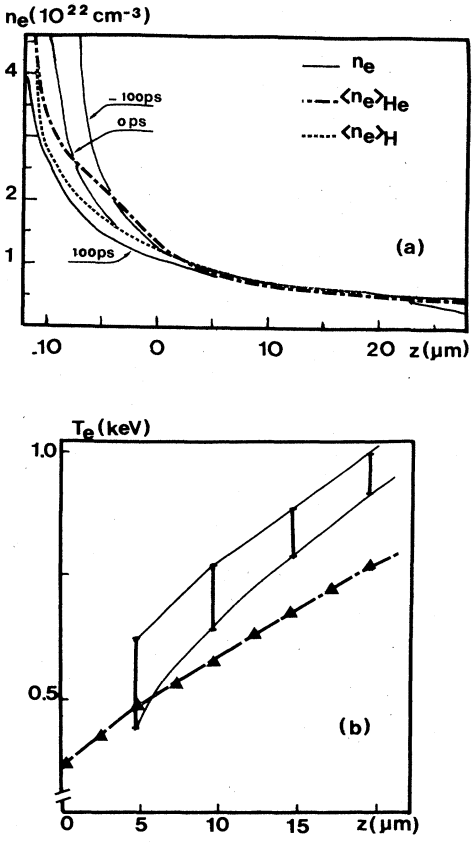

FIG. 6. Code simulation (0.53-μm-3×10^{14}-W/cm^2) showing the effects of time integration on electronic density and temperature measurements. (a) Density profiles. Solid lines: density around the laser pulse maximum (0, ±100 ps). Dashed lines: "weighted" density profiles by He_γ emissivity (long-short dashes) and H_γ emissivity (short dashes). (b) Temperature profiles. Error bars indicate the temperature around the laser pulse maximum (±100 ps). The solid line represents the "weighted diagnostic" temperature deduced from a CRE model, using the ratio of the time integrated populations of the bare and hydrogenic ions.

emissivities, together with the temperature gradient around the laser pulse maximum (-100 ps $\leq \Delta t \leq 100$ ps). Here, time integration effects are added to the non-equilibrium-state systematic error described in Sec. III B. We see that time integration does not affect the results very much, due to the short emission duration. In conclusion, the diagnostic temperature gives results departing from the real temperature by no more than 20—30%, with a systematic underestimate.

IV. EXPERIMENTAL RESULTS

With the methods described previously, we studied the spatial profiles of the line emissivities, of the electronic density, and of the electronic temperature as a function of the laser wavelength and intensity.

A. Laser wavelength effects

We show in Fig. 7 the density and temperature profiles measured for 0.53-μm—3×10^{14}-W/cm^2 and 0.26-μm—1×10^{14}-W/cm^2 laser shots. The comparison is interesting since the density range is identical (the difference of laser intensity is apparently compensated by the difference of wavelength). The maximum density reaches 3×10^{22} cm^{-3} in the two cases. One can notice that the critical density is in the measured range for the uv case. It is clearly evident that the density and temperature gradients are steeper for 0.26-μm laser wavelength. The temperature profile bends slightly around the critical point, in the 700-eV region. Extrapolation in the coronal region gives electron temperatures around 1 keV. However, this has to be confirmed by other experiments due to the insufficient precision of the measurements.

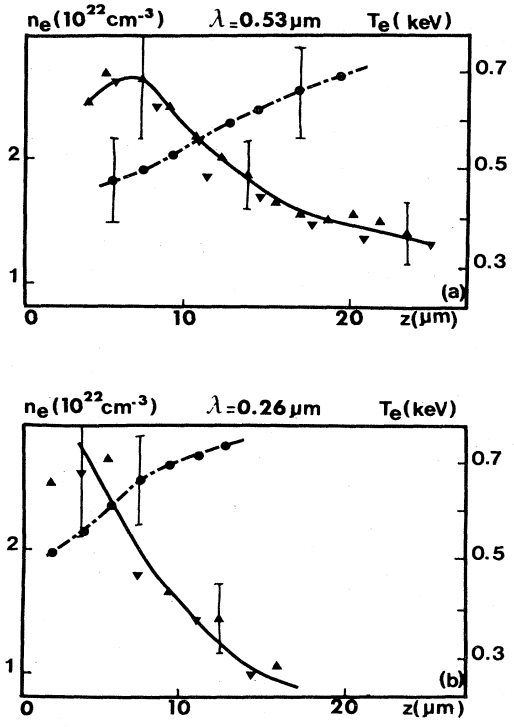

FIG. 7. Experimental electronic density and temperature profiles for 0.53- and 0.26-μm wavelength laser irradiation. Lines are drawn as an aid to the eye, solid line for density, long-short—dashed line for temperature. Density is drawn from two shots represented by different positions of the triangles. (a) 0.53-μm—3×10^{14}-W/cm^2 incident intensity. The long-short—dashed line is the density profile obtained for 1×10^{14}-W/cm^2 laser intensity. (b) 0.26-μm—1×10^{14}-W/cm^2 incident intensity.

B. Laser intensity dependence

Figure 8 shows the density profiles measured for 0.53-μm laser wavelength and for intensities of 3×10^{14} and 1×10^{14} W/cm^2. The electron density is higher and the density gradient is steeper for the greater laser intensity. For the lower intensity, the emissivities were too small to deduce the temperature profile. However, direct comparison of the spatial position of the He_γ and H_γ emissivities shows that the temperature gradient steepens for higher laser intensity. Figure 9 shows the measured He_γ and H_γ emissivities for three laser irradiances (1.1×10^{14}, 1.4×10^{14}, and 3.0×10^{14} W/cm^2). The separation of the He_γ and H_γ emissivity maxima decreases when laser intensity increases. This is characteristic of a steeper temperature gradient because each ionic emissivity peaks for a given temperature. This is clearly evidenced by the simulations in which the maximum of He_γ is obtained at 520-eV electron temperature and H_γ at 1 keV whatever the time, the laser intensity,[15] or wavelength may be.

V. COMPARISON BETWEEN EXPERIMENTS AND SIMULATION

We can get more physical insight from our experimental results by comparing them to code simulations. This determines the parameters of the simulations which give the best agreement. We discuss here the choice of these parameters, i.e., the thermal flux limitation, the geometry, and the laser intensity. Also, we look at the possible reasons for remaining discrepancies. As the experimental

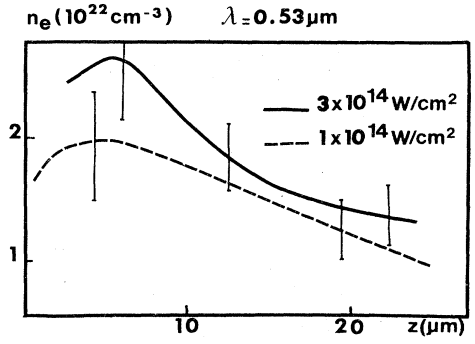

FIG. 8. Measured electron density profiles for varying laser intensity. Laser wavelength is 0.53 μm.

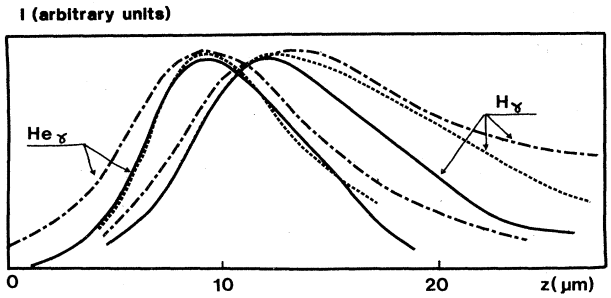

FIG. 9. He_γ and H_γ lines emissivity profiles measured for 0.53-μm wavelength shots at several laser intensities. Solid lines: 3×10^{14} W/cm^2. Short-dashed lines: 1.4×10^{14} W/cm^2. Long-short—dashed lines: 1.1×10^{14} W/cm^2. The origin is shifted to put in coincidence the He_γ line maximum.

results have no absolute spatial origin, we shifted the experimental curves along the laser axis to bring the He_γ emissivity to coincide with the computed one.

Figures 10 and 11 show the experimental electron density and temperature profiles of Figs. 7(a) and 7(b), drawn to a smaller scale, and several computed fits. The simulated electronic density profile is weighted by the He_γ

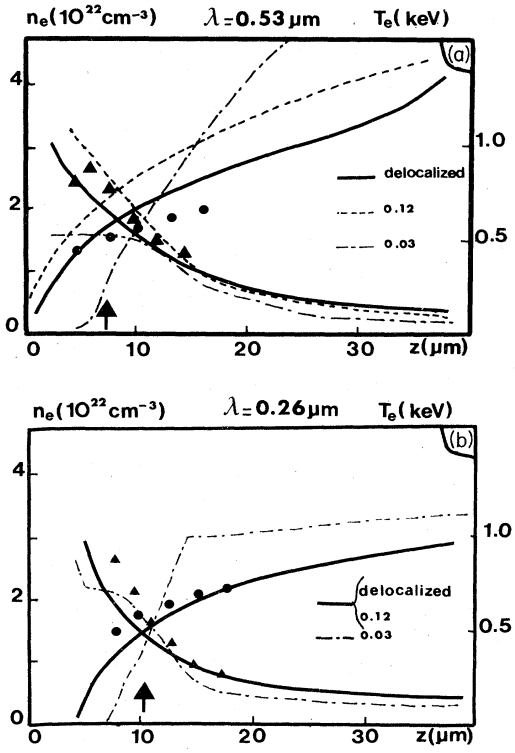

FIG. 10. Comparison of experimental electronic density and temperature profiles to simulations done for variable thermal flux limitation. (a) 0.53-μm—3×10^{14}-W/cm^2 incident intensity, spherical simulation. (b) 0.26-μm—1×10^{14}-W/cm^2 incident intensity, planar simulation. Experimental profiles are represented by triangles (density) and circles (temperature). The different curves correspond to different flux inhibition, i.e., delocalized, $f=0.12$, or $f=0.03$.

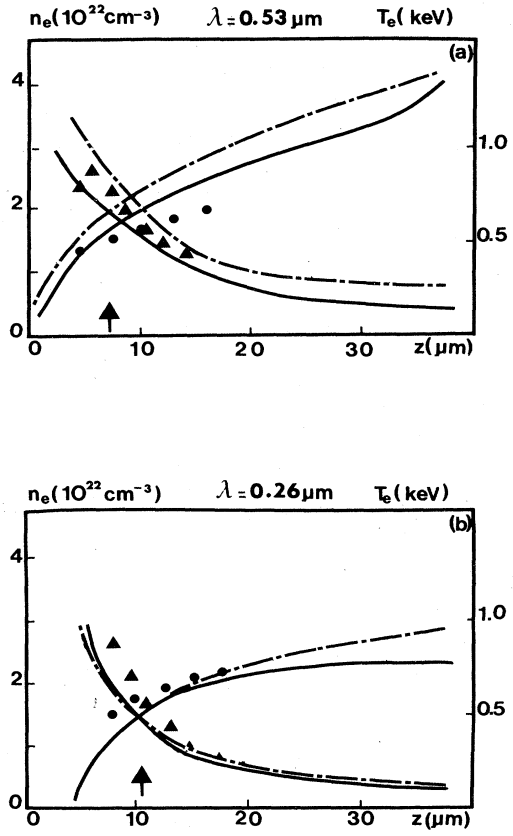

FIG. 11. Influence of the geometry of the simulation on the electron density and temperature profiles. Experimental profiles are indicated by triangles and circles and simulation by lines (solid line, spherical geometry; long-short—dashed line, planar geometry). (a) 0.53-μm laser wavelength, (b) 0.26-μm laser wavelength.

emissivity and time integrated. The electronic temperature profile is calculated at the maximum of the laser pulse. As mentioned before, we expect the experimental temperature profile to be about 20% lower than the calculated one, especially in the outer regions. Transport theory is checked in Fig. 10 and geometric effects in Fig. 11. For 0.53-μm laser wavelength [Fig. 10(a)], the best fit (solid line) has been obtained using the delocalized transport theory,[10] associated with spherical geometry. Long-short—dashed lines show a strong inhibition case ($f=0.03$). Clearly, it does not fit the experiment, as the density profile is too low and the temperature profile too steep. A flux limitation of 0.12 (short-dashed lines) can also explain our data even if it is not the best fit. For the uv case [Fig. 10(b)], very similar conclusions can be derived, but the overall agreement is not as good as in the 0.53-μm case. Delocalized theory and $f=0.12$ flux limitation give exactly the same profiles. The density profile obtained for 0.03 flux limitation is compatible with the experiment but the corresponding temperature profile is still too steep. One can see that the sensitivity of the calculated profiles on the transport flux limitation is weaker for the 0.26-μm case. This is probably due to the fact

that the measured range is no longer centered in the conduction zone but around the critical density.

As we expect that the geometry of the experiment is intermediate between planar and spherical, we have checked the influence of geometry in the simulations. In Fig. 11 we have plotted the profiles computed with delocalized theory and with both spherical (solid lines) and planar (long-short—dashed lines) geometry. Figure 11(a) is drawn for 0.53-μm laser wavelength and Fig. 11(b) for 0.26-μm. It shows that 0.53-μm experiments are better described by spherical geometry and 0.26-μm data by planar geometry. However, in both cases the spatial profiles are less sensitive to geometry than to thermal transport description. As the focal spot is about the same in 0.53- and 0.26-μm cases, we can explain this difference in terms of the penetration of the laser light in the plasma. As the critical density is closer to the solid in the uv case, the conduction zone has a smaller spatial extent along the laser axis and behaves as a planar layer. On the other hand, in the 0.53-μm case critical density lies outwards from the target and the lateral expansion is no longer negligible in the conduction zone.

Some discrepancies remain between experiment and the closest simulation. They can be attributed to uncertainties in the laser intensity fixed in the simulations: As shown in Fig. 12, when we have plotted the weighted density profiles obtained for 1×10^{14}- and 1.5×10^{14}-W/cm^2 laser intensity, the calculated density profiles are very sensitive to the laser intensity used in the simulation. A systematic underestimate of the laser intensity can be a possible explanation of the high measured electron density values. Another explanation may be directly related to the Stark broadening measurements. Indeed, we compare the He$_\gamma$ line profiles to theory for hydrogenlike lines. Overestimates of the electron density can be made if forbidden lines broaden the profile.[16]

Finally, two-dimensional effects can be invoked to explain the decrease of the density near the target. Indeed, if a crater is formed very early during the interaction,[17] the outer regions of the crater can reabsorb the emitted x rays more strongly. The opacity will be very different from its value at the maximum of emissivity, and the "calibration" of the linewidth versus the density may be wrong for this part of the spatial profile.

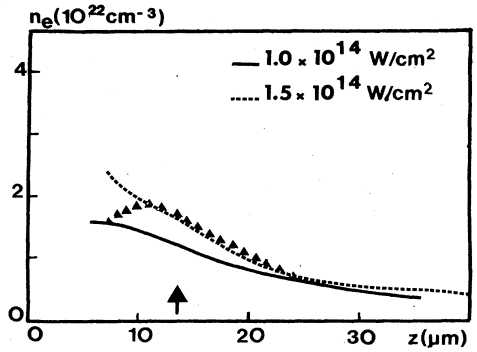

FIG. 12. Sensitivity of the simulation to laser intensity. Comparison of the density profile measured for 0.53-μm wavelength and 1×10^{14}-W/cm^2 incident laser intensity with the simulations calculated for 1.0×10^{14} and 1.5×10^{14} W/cm^2.

VI. CONCLUSION

The use of spot spectroscopy on layered targets and of an imaging knife edge enable one to obtain a sufficient spatial resolution for the determination of electronic density and temperature gradients in the transport region. We have obtained here a set of density and temperature profiles with about 20% precision and 3-μm spatial resolution in the 15-μm-wide region accessible to measurements in our spectral range. We made measurements around the critical surface in the 0.26-μm laser wavelength interaction.

Comparison of experimental profiles and simulations shows that weak flux inhibition (nonlocalized or $f=0.12$) prevails in the conduction region and near the critical density region. Spatial resolution minimizes time integration effects when the emitting zone is moving in the plasma. Indeed, x-ray emissions are strongly peaked at maximum laser irradiance, and spatial resolution seems to be a much more critical point than time resolution in the transport region.

Finally, these experiments not only point to the interest of spectroscopic diagnostics for plasma measurements but also show that the high-density conduction region of a laser plasma is a well-diagnosed x-ray source perfectly suited for high-density detailed spectroscopic studies.

ACKNOWLEDGMENTS

The authors greatly appreciated the help of the GRECO laser staff and the Centre de Densitométrie et de Synthèse d'Images densitometer team. This work has been supported by the Centre National de la Recherche Scientifique.

APPENDIX

We have calculated the optical depth τ_0 and the line intensity attenuation I/I_0 for the He$_\gamma$ and H$_\gamma$ transitions assuming that the plasma is homogeneous and that line profiles are Stark broadened. The optical depth τ_0 is given by

$$\tau_0=\frac{\alpha h}{2m_e}fN(Z,1)D\frac{1}{A},$$

where α, h, and m_e are the fine-structure constant, the Planck constant, and the electron mass; f is the oscillator strength of the considered transition (here $n=4$ through $n=1$); $N(Z,1)$ is the population of the ground level of the Z-time ionized ion; D is the plasma dimension along the line of sight; and A is defined by

$$A=\int\varphi(\nu)d\nu,$$

where $\varphi(\nu)$ is the line profile normalized to $\varphi(0)=1$ (A is of the order of magnitude of the linewidth).

Using Stark profiles calculated by Kepple and Griem[11] we find that A has a very slow temperature dependence and varies as $N_e^{2/3}$. For an electron temperature of 600 eV, we find

$$A(10^{14}\ \mathrm{s}^{-1}) = 4.82 + 0.72(N_e/10^{21})^{2/3}$$

for the He_γ line,

$$A(10^{14}\ \mathrm{s}^{-1}) = 4.99 + 0.58(N_e/10^{21})^{2/3}$$

for the H_γ line,

where N_e is expressed in cm^{-3}.

The plasma is approximated by a 25-μm-thick homogeneous slab, which is a reasonable approximation for a 50-μm-diam cylindrical plasma. We have calculated τ_0 and I/I_0 at the spatial positions corresponding to the maximum emissivity of the He_γ and H_γ lines. We have estimated the populations of the ground states N_{He} and N_{H} from simulations and from a CRE model. Both of these models give $N_{\mathrm{He}} \simeq N_e/Z$ and $N_{\mathrm{H}} \ll N_{\mathrm{He}}$ at the He_γ maximum emissivity and $N_{\mathrm{H}} \simeq N_{\mathrm{He}} \simeq N_e/2Z$ at the H_γ maximum emissivity, Z being the average charge number of the plasma. With these assumptions, we find the following.

(1) At the maximum emissivity of the He_γ line, assuming $N_e = 2\times 10^{22}\ \mathrm{cm}^{-3}$,

$\tau_0 \simeq 6$, $I/I_0 \simeq 0.5$ for the He_γ line,

$\tau_0 \ll 1$, $I/I_0 = 1$ for the H_γ line.

(2) At the maximum emissivity of the H_γ line, assuming $N_e = 10^{22}\ \mathrm{cm}^{-3}$,

$\tau_0 \simeq 1.9$, $I/I_0 \simeq 0.7$ for the He_γ line,

$\tau_0 \simeq 1.2$, $I/I_0 \simeq 0.8$ for the H_γ line.

Thus we find that under our experimental conditions, taking into account opacity effects, the intensity ratio $I_{\mathrm{H}_\gamma}/I_{\mathrm{He}_\gamma}$ is multiplied at worst by a factor of 2 where the He_γ line dominates and is not modified in the outer part of the plasma in the H_γ line emitting zone.

[1] J. D. Kilkenny, R. W. Lee, M. H. Key, and J. G. Lunney, Phys. Rev. A **22**, 2746 (1980).

[2] B. Yaakobi and T. C. Bristow, Phys. Rev. Lett. **38**, 350 (1977); G. Tondello, E. Jannitti, P. Nicolosi, and D. Santi, Opt. Commun. **32**, 281 (1980).

[3] P. G. Burkhalter, M. J. Herbst, D. Duston, J. Gardner, M. Emery, R. R. Whitlock, J. Grun, J. P. Apruzese, and J. Davis, Phys. Fluids **26**, 3650 (1983).

[4] R. W. Lee, J. D. Kilkenny, R. L. Kauffman, and D. L. Matthews, J. Quant. Spectrosc. Radiat. Transfer **31**, 83 (1984).

[5] M. J. Herbst, P. G. Burkhalter, J. Grun, R. R. Whitlock, and M. Fink, Rev. Sci. Instrum. **53**, 1418 (1982).

[6] P. Alaterre, C. Popovics, J. P. Geindre, and J. C. Gauthier, Opt. Commun. **49**, 140 (1984).

[7] P. Alaterre, Thèse de 3e cycle, Paris VI University, 1984.

[8] J. C. Gauthier, J. P. Geindre, N. Grandjouan, and J. Virmont, J. Phys. D **16**, 321 (1983).

[9] F. Amiranoff, R. Fabbro, E. Fabre, C. Garban-Labaune, and M. Weinfeld, J. Phys. (Paris) **43**, 1037 (1982); F. Amiranoff, Thèse d'Etat, Paris XI University, 1984.

[10] J. F. Luciani, P. Mora, and J. Virmont, Phys. Rev. Lett. **51**, 1664 (1983).

[11] P. C. Kepple and H. R. Griem, NRL Report No. 3634, 1978 (unpublished).

[12] R. Cauble and H. R. Griem, Phys. Rev. A **27**, 3187 (1983).

[13] B. D'Etat, in *Proceedings of the Seventh International Conference on Spectral Line Shapes, Aussois, 1984* (De Gruyter, Berlin, in press).

[14] H. R. Griem, *Plasma Spectroscopy* (McGraw-Hill, New York, 1964).

[15] P. Alaterre, C. Popovics, J. C. Gauthier, and J. P. Geindre, GRECO ILM Annual Report, 1983, p. 218 (unpublished).

[16] R. W. Lee, G. E. Bromage, and A. G. Richards, J. Phys. B **12**, 3445 (1979).

[17] C. Randall and J. S. Degroot, Phys. Rev. Lett. **42**, 179 (1979); P. C. Thompson and P. D. Roberts, Laser Part. Beams **2**, 13 (1984).